Deep seismic faulting triggered by nano-crystallization of wadsleyite from olivine

T. Ohuchi[1]*, Y. Higo[2], Y. Tange[2], T. Sakai[1], and T. Irifune[1,3]

[1]Geodynamics Research Center, Ehime University, Matsuyama 790-8577, Japan

[2]Japan Synchrotron Radiation Research Institute, Sayo, Hyogo 679-5198, Japan

[3]Earth-Life Science Institute, Tokyo Institute of Technology, Tokyo 152-8550, Japan

*Corresponding author

Phone: +81-89-927-8159 Fax: +81-89-927-8167

E-mail: ohuchi@sci.ehime-u.ac.jp

Activity of deep earthquakes, which increases with depth from ~400 km to a peak at ~600 km and abruptly decreases to zero at 680 km, is enigmatic, because brittle failure is unlikely to occur under the corresponding pressures of 13−24 GPa. It has been suggested that pressure-induced phase transformations of olivine in subducted slabs are responsible for occurrence of the deep earthquakes, based on deformation experiments under pressure. However, most experiments were made using analogue materials of mantle olivine and at pressures below ~5 GPa, which are not applicable directly to the actual slabs. Here we report the results of deformation experiments combined with in situ X-ray observations and acoustic emission measurements on $(Mg,Fe)_2SiO_4$ olivine at 11−17 GPa and 960−1250 K. We find that shear cracking followed by rapid formation of nano-crystalline wadsleyite on the crack surface is essential for the occurrence of faulting, which is observed only at temperatures around 1160 K. The faulting is accompanied by intense acoustic emissions and partial melting, which is likely to be induced by rapid sliding and adiabatic shear heating along the weak layer of nano-crystalline wadsleyite. In contrast, the olivine to ringwoodite transformation in $(Mg,Fe)_2SiO_4$ olivine would not cause such faulting because of the slow diffusion creep of ultrafine-grained ringwoodite. Our findings suggest the transformational faulting occurs on the surface of the metastable olivine wedge in subducted slabs, leading to deep earthquakes in the limited depth range.

$(Mg,Fe)_2SiO_4$ olivine is the major mineral in the Earth's mantle and subducting slabs, which shows successive phase transformations to wadsleyite (at pressure around 13 GPa)

and ringwoodite (~20 GPa) with modified spinel and spinel structures, respectively, and decomposes into an assemblage of bridgmanite + ferro-periclase (~24 GPa) with increasing pressure. The concept of transformational faulting upon the phase transformations of olivine, which is triggered by propagation and linking-up of lends-shaped 'anticracks' along the direction of the maximum shear stress, has been widely accepted to explain faulting in the mantle transition zone (410−660 km in depth), based on experimental studies on a germanate analogue (Mg_2GeO_4)[1-3] and ice[4]. The anticrack is assumed to be filled with a nanocrystalline aggregate of the high-pressure phases, which behaves as a low-viscosity fluid due to grain-size-sensitive creep[2,3,5]. However, the hypothesis of anticracks needs to be reconsidered because the majority of the sources of acoustic emissions (AEs) in the transforming olivine associates no volumetric strain[3], inconsistent with the volume compaction expected in this model. Moreover, Mg_2GeO_4 olivine, which transforms to the spinel structure at 1−2 GPa, has been used due to the limitation of pressures available in conventional deformation apparatus to ~5 GPa. However, this may not be an adequate analogue[6] because Mg_2GeO_4 olivine transforms directly to the spinel phase without passing through the modified spinel phase. A recent study on fayalite (Fe_2SiO_4)[7] confirmed that the transformational faulting can be initiated by the olivine-spinel transformation but suggested that development of the fault slip requires an additional mechanism such as adiabatic instability[8-10]. However, it is unclear whether phase transformations of olivine can trigger adiabatic instability, because it has been difficult to perform well-controlled deformation experiments with in-situ

monitoring of dynamic behaviors of the sample under the conditions of the mantle transition zone.

We performed synchrotron in-situ deformation experiments on sintered body of a natural olivine powder with a composition of $Mg_{1.8}Fe_{0.2}SiO_4$ (hereafter, OL100 sample). We also used sintered aggregate of a 92:8 mixture of this olivine and natural orthoenstatite powders (OL92). Deformation runs were conducted at 11−17 GPa and 960−1250 K using a deformation-DIA apparatus (Extended Data Fig. 1). X-ray radiographs of the sample under deformation were taken to verify the occurrence of faulting in the sample (Fig. 1). Evolutions of differential stress, pressure, strain, and acoustic activity with time for deforming samples are shown in Fig. 1a and Extended Data Figs. 2-3. Differential stress was almost constant at strains of >0.1 and pressures of >11 GPa (i.e., wadsleyite/ringwoodite stability field)[11] in all of the runs. Intensity of the 240 diffraction peak of wadsleyite (hereafter, Wad_{240}), which indicates the presence of more than ~5 vol.% of wadsleyite in the sample (Extended Data Table 1), was sensitive to not only temperature but also the P-T-t path before the sample deformation (see Methods). For the P-T-t path#1 (the deformation started in the stability region of olivine, where the pressure was increased gradually by 2−3 GPa to those of the wadsleyite region), the Wad_{240} peak was detected only at 1250 K, while it was absent at lower temperatures. A tiny amount of wadsleyite (0.1−0.2 vol.%) was found in two of the recovered samples deformed at 1160 K (M2676 and M3101), but no wadsleyite was observed in the samples deformed at lower temperatures (Extended Data Table 1). The Wad_{240} peak was detected from the samples

deformed at 1160 K for the P-T-t path#2 (over-pressurized just before the deformation to enhance nucleation of wadsleyite) or #3 (formation of wadsleyite in its stability field before the deformation). Yield strengths of our samples are significantly lower than the steady-state creep strength of sintered olivine[12,13] (Fig. 2a), and are close to that of powdered (i.e., highly-fractured) olivine[14].

Acoustic activity shows a negative temperature dependence regardless of the occurrence of phase transformation of olivine, which becomes almost silent due to microcracking-free plastic flow at temperatures above 1200 K (Fig. 2b). The averaged AE rates (N_{in}/ε_t) of the faulted samples are equivalent to or smaller than those of the fault-free samples (Fig. 2b), showing that the AE rate is not strongly correlated with the occurrence of faulting. The first motion at each AE sensor shows that most of the AE events are of a double couple (i.e., both positive and negative polarities) with a limited number of isotropic compaction (i.e., negative polarities)[15] (Fig. 1a and Extended Data Figs. 2-3). This indicates that anticracks[2] are not directly associated with the AE source, because they should lead to the compaction by the olivine-wadsleyite transformation with a volume reduction of ~7 vol.% (ref.[16]), which is consistent with the result of an earlier study for germanate olivine[3]. Our results are also consistent with the focal mechanism of deep earthquakes which have no significant isotropic components[8]. The AEs from inside of the samples are concentrated at strains less than 0.2, while virtually no AEs are observed at higher strains due to aseismic plastic deformation of the sample without faulting (Extended Data Figs. 2-4).

In the deformation stage of M2676 and M3100 conducted at 1160 K, the semi-brittle flow was terminated by faulting followed by a sudden large pressure drop (blow-out), while no faulting was observed in other 11 deformation runs. Yield strength of the faulted samples (1.5−1.8 GPa) is lower than that of many other samples deformed at 1160 K (Fig. 2a), suggesting that larger stress is not necessarily required for the occurrence of faulting. In these two runs with faulting, intense AEs (amplitude >1V) are radiated not only from inside but outside of the sample, and the hypocenters locate along the fault plane crossing the sample (Fig. 1b and Extended Data Fig. 4f), showing occurrence of a fault-slip associated rupture. A shear crack, which occurred 9 minutes before the rapture in M2676 (at a strain of 0.14: Fig. 1), is thought to be the precursor of the faulting.

A throughgoing faults with an angle of ~50° to the compression direction occurred in the OL92 sample of M2676. The fault has a displacement of ~500 μm and is filled with a gouge layer having a thickness of 5−20 μm (Figs. 3a-b). Transmission electron microscope (TEM) observations of a foil fabricated using a focused-ion beam (FIB) revealed that the gouge consists of round-shaped olivine/wadsleyite grains (20−300 nm in diameter), platinum blobs (10−500 nm) and an interconnected melt-like phase (Fig. 3c). No micrometric wadsleyite grain was observed in off-fault intact domains of the sample. The melt-like phase is amorphous (Figs. 3d-e), which is enriched in silicon, calcium and iron (SiO_2 = 54−62 wt.%; CaO ~4 wt.%; FeO/MgO ~0.5: Extended Data Fig. 5a), and is explained by low-degree (<40 wt.%) partial melting of dry lherzolite[17] above 2170 K at 13 GPa (Extended Data Fig. 1a)[18]. The presence of platinum blobs strongly

123 suggests melting of platinum strain marker during the faulting, also indicating generation
124 of such a high temperature. The ultrafine grains of olivine found in the gouge should be
125 the back-transformation product of wadsleyite under the instantaneous high temperature
126 in olivine stability field[19] (Extended Data Fig. 1a).

127 A pair of conjugate throughgoing faults with an angle of 20−30° to the compression
128 direction occurred in the OL100 sample recovered from another run accompanied by
129 faulting (M3100) (Extended Data Figs. 6a-c), where the displacement of the fault ranges
130 from 50 to 100 μm. Off-fault damage zone is observed on both sides of the fault, which
131 consists of broken fragments of olivine grains. Silicon-rich patches (SiO_2 = 62−84 wt.%)
132 are observed in ultrafine-grained domains, mainly made of wadsleyite/ringwoodite
133 nanograins (typically ~20 nm in diameter) (Extended Data Figs. 5b and 6d-e). Iron-rich
134 nanoparticles (FeO = 14−27 wt.%) are also distributed near the ultrafine-grained domains.
135 Formation of both the silicon-rich and iron-rich phases can be explained by incongruent
136 melting of wadsleyite/ringwoodite to an iron-rich liquid and stishovite (SiO_2) at a peak
137 temperature of >2500 K at 15.5 GPa (Extended Data Fig. 1a)[20]. Thus, both M2676 and
138 M3100 with faulting show evidence of suffering very high temperature above ~2200 K
139 in the limited regions along the faults, suggesting generation of instantaneous high
140 temperature by adiabatic shear heating upon faulting.

141 In general, mode-II shear cracks can be formed by the coalescence of interacting
142 mode-I (opening mode) tensile cracks[21] occurring at the initial stage of brittle failure[22].
143 Considering that volume expansion by opening of mode-I cracks is inhibited at elevated

144 pressures, nucleation and propagation of mode-II cracks would proceed without the
145 process of mode-I cracking in our experiments. In the M2955 sample deformed at 1160
146 K, a mode-II throughgoing crack having a very limited amount of slippage (~10 μm:
147 Extended Data Figs. 6h-j) is filled with broken fragments of olivine (20−100 nm in
148 diameter), but no high-pressure phases of olivine are observed. Yield strength of this
149 sample (~2.4 GPa) is significantly higher than that of the faulted samples (1.5−1.8 GPa
150 at 1160K)(Fig. 2a), suggesting that fault slip requires some "lubricant" (i.e., grain-size-
151 sensitive creep of a nanocrystalline aggregate of wadsleyite/ringwoodite) on the crack
152 surface, as is the case for M2676 and M3100.

153 We estimate the nucleation rate of wadsleyite ($\dot{N}$) and the rate constant of the olivine-
154 wadsleyite phase transformation (k) for two typical pressures of 13 and 15.5 GPa in the
155 wadsleyite stability field assuming that preferential nucleation proceeds on the crack
156 surface[23] (see Supplementary Information). The results (Extended Data Fig.7) show that
157 the interfacial nucleation of wadsleyite is effective in a narrow temperature window of
158 ~1160 K at 13 GPa on crack surfaces, while the transformation on both grain boundaries
159 and crack surfaces is accelerated with increasing temperatures at 15.5 GPa. As
160 microcracking would not occur at temperatures above 1200 K, indicated by the very low
161 values of the AE rate (Fig. 2b), the maximum transformation rate on crack surfaces should
162 be realized at ~1160 K under these pressures, consistent with the observation of faulting
163 only in the runs at this temperature.

164 Elastic energy stored in a viscoelastic material may be spontaneously released at the

seismic strain rate by high-temperature self-localizing thermal runaway[10]. A theoretical study actually shows the possibility of frictional melting during the rupture of the 1994 Bolivian earthquake (depth =637 km)[24]. The critical strain rate $\dot{\varepsilon}_c$, which is required for the adiabatic instability, is expressed as follows[25]:

$$\dot{\varepsilon}_C \sim \frac{h\rho c_p \kappa R T^2}{\sigma H^* L^2} \quad (1)$$

where h is work hardening coefficient (=1), ρ is density (=3.6 g· cm^{-3} at 13.5 GPa)[26], c_p is specific heat (=817 J· kg^{-1}K^{-1})[27], κ is thermal diffusivity (=0.7 mm^2· s^{-1})[28], H^* is activation enthalpy for deformation (=907 kJ· mol^{-1} for the Peierls creep at 13.5 GPa)[12,29], and L is sample size (=1.2 mm in length). Substituting these parameters of olivine for Eq. (1), we obtain a critical strain rate of 1.2×10^{-2} s^{-1} at a differential stress of 1.5 GPa to initiate adiabatic shear heating at the background temperature of 1160 K (Fig. 4a). Instantaneous strain rate of the damage zone (or gouge layer) (thickness L_d ~20 μm: Extended Data Fig. 6b) may reach ~0.1−2 s^{-1} during the faulting of ~10 s, as estimated from the stroke sensors of the anvils in M2676 and M3100, under the assumption that strain was localized with a factor of L/L_d. Thus, the adiabatic instability can be initiated by rapid nucleation of wadsleyite on crack surface followed by diffusion creep of wadsleyite[30] with grain sizes of ~20 nm (Fig. 4b and Extended Data Fig. 6e).

It has been reported that the latent heat release associated with phase transformation enhances deep earthquake activity[31,32]. A net temperature increment ΔT by the latent heat release across the phase transformation is given as[33]:

$$\Delta T \sim \frac{-(T\Delta S_r + \Delta G_v)}{C_p} \quad (2)$$

where ΔS_r is the entropy change of reaction, ΔG_v is the free energy change of reaction, and C_p is isobaric heat capacity. ΔG_v is approximated as $\Delta P \cdot \Delta V/V_0$, where ΔP is the overpressure from the equilibrium and $\Delta V/V_0$ is the fractional volume change[16]. Eqs. (1) and (2) show that phase transformation of metastable olivine at higher pressures is effective in initiating adiabatic instability due to positive temperature dependence of strain rate. For the olivine-wadsleyite transformation at 1160 K, the ΔT is evaluated as ~60 and ~110 K for the confining pressure of 13 and 15.5 GPa, respectively. Assuming that nucleation of wadsleyite proceeds much faster than the conductive heat transfer[33], strain rate can reach the critical strain rate for the adiabatic instability at a lower stress level (~0.5 GPa: Fig. 4a). Considering that theoretical studies predict high stress magnitudes up to ~2 GPa (ref.[34]) due to accumulation of strain in the deep seismic zone[35], deep earthquakes triggered by the adiabatic instability may occur without the aid of latent heat release upon the olivine-wadsleyite transformation (Fig. 4a). In contrast, the diffusivity of silicon in ringwoodite[36] predicts that diffusion creep of ultrafine-grained ringwoodite is too slow to induce the adiabatic instability (Fig. 4a) even if superheating by the transformation of metastable olivine to ringwoodite (ΔT ~200 K at 20 GPa)[33] is taken into account. Thus, it is suggested that the olivine to ringwoodite phase transformation would not cause faulting and hence deep earthquakes.

Seismic imaging of the deep mantle demonstrates the presence of metastable olivine wedge (MOW), accompanied by deep earthquakes, as a low-velocity zone with a thickness of tens of kilometers inside the cold slab[37,38]. The present study suggests that

the deep earthquakes occur when the temperature of the MOW reaches those close to 1160 K, where the nano-crystallization of wadsleyite occurs followed by the faulting due to shear instability, although this critical temperature may be slightly lower in the geological time scale (Extended Data Fig. 7). In fact, the observed deep earthquakes are reported to locate along an isotherm of ~1000 K in deep slabs[39]. It has been widely recognized that some characteristics of deep earthquake, such as the frequency of aftershocks and the Gutenberg-Richter b-value, reflect thermal structures of deep slabs[8]. The very small aftershock rate and higher b-values of deep earthquakes in warmer slabs[40] can be attributed to a smaller number of the earthquake nucleation in their thinner MOW[41]. Numerical studies based on experimental kinetic data show that metastable olivine in cold slabs probably persist to depths of ~600 km, below which ringwoodite is the major phase down to ~700 km (ref.[8,42]). Our results show that the deep earthquakes in the mantle transition zone is mainly caused by the metastable olivine to wadsleyite transformation along the isothermal regions in the MOW, and the corresponding transformation to ringwoodite would play no major roles in occurrence of the deep earthquakes, consistent with the rapid decrease in seismicity from ~600 km to 680 km (ref.[43]).

Figure legends

Figure 1 | Mechanical and acoustic records in the OL92 sample faulted at 1160 K (M2676). a, The stress values were obtained from three diffraction peaks of olivine (diamond: 021, square: 101, triangle: 130). Pressure and strain are shown by gray open circles. The cumulative number of AEs (gray line), amplitudes (red impulses: AEs from the inside of the sample; green: outside of the sample), and the average of polarity values are plotted against time. The total number of AE events (N_{in}: from the inside of the sample: N_{out}: outside of the sample) is also shown. The timings of shear cracking, rupture, and blow-out are shown by thin-dashed, thick-dashed and dotted lines, respectively. **b**, Two-dimensional views of AE hypocenters in the deforming sample (blue cylinder) and the pressure medium (black square) during periods of each 5 (or 2) minutes. The black cross shows typical errors for the location of hypocenter. A brown-dashed line shows the seismic plane observed at the timing of rupture. Arrows represent the compressional direction. **c**, X-ray radiographs of the deforming sample at each strain ε. Positions of platinum strain markers are shown by arrows. Splitting of the middle strain marker (ε =0.14 at 62 min) suggests shear cracking followed by faulting. Direction of the incident X-ray is perpendicular to the radiograph images.

Figure 2 | Summary of yield strength (σ_y) and averaged AE rate (N_{in}/ε_t). a, Temperature dependence of σ_y of the samples (solid: OL100, open: OL92). Large symbols represent the samples with faulting (M2676 and M3100). Creep strength of olivine (Ol)

is calculated assuming the Peierls creep (for sintered aggregates[8,13]; highly-fractured powdered samples[14]), wet dislocation (disl.) creep[29]; wet dislocation-accommodated grain boundary sliding (dislGBS; for a typical grain size of 10 μm)[44]. The brown area represents the range of temperatures at which no nucleation of wadsleyite was observed in the recovered samples. **b**, Temperature dependence of N_{in}/ε_t, where N_{in} is the total number of AE events in the sample and ε_t is the total strain.

Figure 3 | Microstructures of the OL92 sample faulted at 1160 K (M2676). a, A secondary electron image of the recovered sample. The fault is highlighted by a red dashed line. **b**, A magnified image of the fault (yellow square in a). **c**, A STEM image and element maps showing the gouge layer in the fault. In the element maps, grayscale corresponds to concentration of elements (pink: magnesium; green: iron; blue: silicon; yellow: calcium). Platinum (Pt) and nickel (Ni) blobs are distributed along the network of the amorphous phase. The FIB foil was prepared from the area shown in b (yellow square). **d**, A TEM image of a wadsleyite (Wad) next to an amorphous pocket in the fault gouge. **e**, A high-resolution TEM image showing the boundary between the wadsleyite grain and the amorphous pocket.

Figure 4 | Occurrence of transformational faulting under conditions of the mantle transition zone. a, Conditions for localized heating in metastable olivine at pressures of 13−15.5 GPa and the background temperature of 1160 K. The thick-solid curve shows

the critical strain rate for the adiabatic instability, where deformation of the wall rock is controlled by the Peierls creep[12,13]. Long-dashed curves represent the creep strength of ultrafine-grained wadsleyite (grain size of 20 nm) without (ΔT =0 K) and with (=60 K at 13 GPa; 110 K at 15.5 GPa) the effect of superheating (Eq. 2). Dot-dashed curves are the corresponding estimates for ringwoodite. Our experimental results at 1160 K are shown by symbols. Crosses show the estimated strain rate at the timing of faulting (see text). **b**, Schematic illustration of the present transformational faulting model. At the temperatures of ~1160K, shear cracking is followed by a rapid nucleation of nano-crystalline wadsleyite on the crack surface. Diffusion creep of such fine-grained wadsleyite induces shear localization associating localized heating.

Acknowledgements

We thank X. Lei for his technical support for AE monitoring. This research was conducted under the approval of SPring-8 (Nos. 2018B1052, 2019A1731, and 2019B1115) and supported by the Grant-in-Aid for Scientific Research (Nos. 16H04077, 18K18788, and 19H00722).

Author contributions

T.O. conceived the idea, conducted experiments, and wrote the manuscript. T.S. contributed to TEM foil fabrication. Y.H., Y.T. and T.I. contributed to in-situ experiments and discussion.

287

288 **Competing interests**

289 The authors declare no competing interests.

290

291 # Methods

292 **Starting material and deformation experiments**

293 The starting material and the procedure for synthesis of OL100 and OL92 samples
294 are the same as those in our previous study[45]. The fine-grained powder of olivine (from
295 San Carlos, USA) or a mixture of 92 wt.% olivine and 8wt.% orthoenstatite (from
296 Kilosa, Tanzania) was put into a nickel capsule (inner diameter: 8 mm; length: 11 mm).
297 The olivine and olivine-orthoenstatite powders were sintered at 4 GPa and 1073 K for
298 1.5 hour using a Kawai-type multi-anvil apparatus at Ehime University. The average
299 grain size of olivine in the sintered sample is ~15 μm. The sintered sample was core-
300 drilled to a rod with a diameter of 1 mm and a length of 0.6 mm. Melting of the OL100
301 and OL92 samples is used for estimation of a peak temperature during faulting (e.g.,
302 OL100: >2500 K at 15.5 GPa; OL92: ~2170 K at 13 GPa)[18,20]. Mechanical behavior of
303 the OL92 sample was found to be almost the same as that of the OL100 sample because
304 92 wt.% of olivine forms the load-bearing framework[46], suggesting that the present
305 discussion and conclusions are independent on these two samples.

306 We conducted deformation experiments on the OL100 and OL92 samples using a
307 deformation-DIA apparatus combined with the large-volume MA-6-6 system at the

BL04B1 beamline of SPring-8. A semi-sintered cube of cobalt-doped magnesia with an edge length of 5 mm was used as the pressure medium, which was surrounded by five tungsten carbide anvils (with a truncated edge length of 3 mm) and an X-ray transparent cubic boron nitride (cBN) (or sintered diamond) anvil placed on the down-stream side. Two of the four sliding blocks on the down-stream side have a conical X-ray path with a maximum 2θ angle of ~10º. Two core-drilled samples were placed along the compression direction, and the samples were separated by a 10 μm-thick platinum strain marker. The cored samples, which were sandwiched in between two hard-alumina pistons with a diameter of 1 mm and a length of 0.3 mm, were placed in a nickel capsule (outer diameter: 1.1 mm; wall thickness: 0.05 mm; length: 1.8 mm) (Extended Data Fig. 8a). The hard-alumina pistons were coated with platinum (thickness of a few hundred nanometers) to avoid chemical reaction between the pistons and the samples. Each piece of sample/piston was separated by a platinum strain-marker having a thickness of 10 μm. The nickel capsule surrounded by a magnesia (MgO) sleeve was inserted in the inner bore of a boron nitride composite heater (TiB_2 + BN +AlN)[47], which was placed in the $LaCrO_3$ thermal insulator. Small portions of the pressure medium and the $LaCrO_3$ thermal insulator along the X-ray path (a diameter of 1.4 mm) were replaced by an amorphous boron powder cemented with epoxy resin (at a ratio of 4:1 by wt.) to maximize the intensity of the diffracted X-rays.

The cell assembly was first pressurized hydrostatically up to 0.6 MN in the main-ram load and temperature was raised to 1470 K at a rate of ~50 K/min. A thermocouple

was not used in the deformation experiments because the thermocouple damaged the truncated surface of cBN (or sintered diamond) anvils at high temperatures. Temperature was estimated from the relationship between temperature and power established for a $W_{97}Re_3$-$W_{75}Re_{25}$ thermocouple placed along one of the diagonal directions of the cell assembly (Extended Data Fig. 8b). Temperature around the outer wall of the nickel capsule samples was monitored in the series of calibration experiments. The uncertainties in temperature estimate in this study is ±60 K.

The pressure-temperature-time (P-T-t) paths of all experiments in relation to the olivine-wadsleyite-ringwoodite equilibrium phase boundaries[11] are shown in Extended Data Fig. 1. We adopted three P-T-t paths before the deformation stage: i) path#1; the sample was annealed at 1470 K and pressures below 12 GPa in the olivine stability field[11] for 20 minutes to decrease the density of defects and microcracks created during the cold-compression stage (M2600, M2673, M2676, M2880, M2955, M2957−2959 and M3101). ii) Path#2; the annealing procedure of the path#1 was followed by hydrostatic pressurization (up to 0.85−1 MN) at 860 K to avoid the pressure-induced transformations of olivine before the deformation stage (M3078 and M3100). iii) Path#3; the sample was annealed at 1470 K and 13−13.5 GPa in the wadsleyite stability field[11] for 20 minutes before the deformation stage (M2670 and M2672), where olivine partially transformed to wadsleyite with grain sizes of 2−5 μm.

In all of these runs with three P-T-t path, the sample was subsequently deformed in the uniaxial compression geometry at a constant stroke rate (2−4 μm/min) by advancing

350 the upper and lower first-stage anvils. Temperature was kept constant (960−1250 K)
351 during the deformation stage. Pressure was gradually increased above the phase
352 boundary between the olivine stability field and the olivine+wadsleyite coexisting
353 field[11] during the early deformation stage in the path#1. We tried to keep the pressure
354 within the wadsleyite stability field at higher strains by increasing the main-ram load
355 (+0.1 to +0.3 MN/hour) during the deformation stage, as some pressure drop with
356 increasing strain was observed in five deformation runs (M2670, M2880, M2955,
357 M2957 and M2959).
358
359 **X-ray data analysis**
360 Two-dimensional radial diffraction patterns of monochromatic X-rays (energy 60
361 keV) were taken by using a MAR-CCD camera with 8−9 minutes of exposure time. The
362 half-circle radial diffraction patterns were subdivided into 18 sectors having a uniform
363 azimuth angle of 10°. Peak positions of four diffraction peaks of olivine (*hkl* = 020, 021,
364 101, and 130: Extended Data Fig. 8c) in each subdivided sector were semi-
365 automatically determined in pressure and stress measurements. Pressure was determined
366 from the unit-cell volume, which can be calculated from the *d*-spacing under hydrostatic
367 conditions, based on an equation of state of olivine[48]. Differential stress was estimated
368 from the azimuth angle dependency of the *d*-spacing[49] using olivine single-crystal
369 elastic constants[26,50]. The uncertainty of the stress resulting from the accuracy of the
370 measurements is defined as the 1-sigma in the least square fit of the Singh's theoretical

curve of the azimuth angle dependency of *d*-spacing. A diffraction peak of wadsleyite (*hkl* =240: Extended Data Fig. 8c) was used for in-situ identification of wadsleyite. A comparison of the diffraction dataset and microstructures of the recovered samples showed that the peak was detectable when the volume fraction of wadsleyite is higher than 5 vol.%.

The strain ε of a deforming sample was evaluated from the distance between two platinum strain-markers placed between the sample and an alumina piston, which was monitored by in-situ monochromatic X-ray radiography. Each radiograph image (30 seconds of exposure time) was taken just before the acquisition of the 2-D X-ray diffraction pattern. Natural strain (i.e., $\varepsilon = -ln\ (l/l_0)$, where l_0 is the initial length of the sample; l: the length of the sample during deformation) was adopted to evaluate the sample strain. The uncertainty in the strain mainly due to the shape of strain marker is within 10%. A sudden splitting of a platinum strain marker monitored by in-situ observations was interpreted as the occurrence of faulting[45], which was confirmed in the recovered sample.

AE monitoring and data processing

We monitored AEs as a proxy of fracture propagation at high pressure and temperature. AE monitoring was combined with in-situ X-ray diffraction/imaging analysis during the stage of deformation. The setup and procedure for AE monitoring are based on those in previous studies[15,45]. AE events were collected with the six

392 piezoceramic lead-zirconate titanate transducers (PZT) that were attached to the sides of
393 the second-stage tungsten carbide anvils (Extended Data Figs. 8d-e). Each transducer,
394 having a size of 4 mm in diameter and an ~0.5 mm thickness (resonant frequency of ~4
395 MHz) was electrically isolated from the second-stage anvils by a mirror-polished
396 alumina wear plate (0.5 mm thick). The raw acoustic signals were amplified by ultra-
397 small pre-amplifiers (20 dB gain), which located near the transducers (distance of ~140
398 mm from a transducer) and the amplified signals were again amplified by low-noise 30
399 dB pre-amplifiers. Use of the ultra-small pre-amplifiers significantly reduced the
400 electrical noise in the synchrotron laboratory environment on the signals, resulting in
401 improvement of the signal-to-noise ratio (i.e., S/N) of waveforms (Extended Data Fig.
402 8f). The doubly-amplified signals having a maximum amplitude of >80 mV were
403 recorded using a high-speed multi-channel waveform recording system at a sampling
404 rate of 100 MHz (16 bit, 8192 samples). The P-wave arrival time was determined based
405 on the Akaike Information Criterion approach[15,51] for each waveform. The P-wave
406 arrival time was corrected by substituting the travel time of the P-wave thorough a WC
407 anvil (= D/v_{pa}, where D is the distance between the 2nd-stage anvil top and the
408 transducer; v_{pa}, P-wave velocity in the anvil), prior to calculation of the hypocenter
409 location. P-wave velocity of the WC anvil (6.6 km/s) is assumed to be constant
410 throughout the high-pressure experiments. We define the positive and negative polarities
411 of the first motion of waveforms as +1 and -1 in this study. The average of the polarity
412 values for all sensors was calculated to constrain the focal mechanism. Following the

definition of the body-wave earthquake magnitude, the relative magnitude (M_{ae}) of an AE event is determined according to the logarithm of the maximum amplitude of the AE signal (V_{max}) detected on a chosen channel[52], that is, $M_{ae} = log_{10}V_{max}$.

Hypocenter locations were calculated from the difference in the arrival time between the 1st and i-th transducers ($t_i - t_1$) as a function of the true hypocenter location X' ($x+dx, y+dy, z+dz$), the tentative hypocenter location X (x, y, z) and the location of the i-th transducer P_i (a_i, b_i, c_i) ($i = 1, 2\cdot\cdot\cdot, 6$):

$$\left(\frac{x-a_i}{R_i}-\frac{x-a_1}{R_1}\right)dx+\left(\frac{y-b_i}{R_i}-\frac{y-b_1}{R_1}\right)dy+\left(\frac{z-c_i}{R_i}-\frac{z-c_1}{R_1}\right)dz=v_p(t_i-t_1)-R_i+R_1 \quad (3)$$

where v_p is the averaged P-wave velocity in the sample, and R_i is the distance between X and P_i. In the calculation, we obtained the best location of X' that gives the minimum residual of Eq. (3) under the assumption that the velocity structure of the cell assembly was homogeneous and the averaged P-wave velocity was equal to that for olivine (e.g., 9.1 km·s^{-1} at 14 GPa and 1160 K)[48] in the cell assembly. In this study, the location uncertainty is defined as the root mean square of the right side of Eq. (3).

Micro- and nanostructural observations and water content measurement

The recovered cell assembly was cut with a low-speed saw to obtain the sectioned plane parallel to both the directions of axial compression and the incident X-ray. The sectioned samples were impregnated with epoxy under a vacuum and then polished using alumina powder followed by colloidal silica suspension. Backscattered electron (BSE)

434 images of the polished surface of the recovered samples were taken using a JEOL JSM-
435 7000F field-emission scanning electron microscope (FE-SEM) equipped with an EDS
436 detector. The chemical compositions of minerals were measured under the operating
437 conditions of 15 kV accelerating voltage and 1 nA probe current. Submicron-scale
438 microstructures around the faults (or a mode-II crack) in three samples (M2676, M2955
439 and M3100) were also examined by using a field-emission scanning TEM (STEM) JEOL-
440 2100F equipped with a JEOL EDS detector system at Ehime University operated at 200
441 kV accelerating voltage. Thin foils (thickness of ~100 nm) were prepared using a focused
442 ion beam system (FEI Scios) with an accelerating voltage of 30 kV. Characteristic X-rays
443 detected by the STEM/EDS were used to analyze the compositions, where the EDX
444 spectra were acquired for 30 seconds for each analysis. The chemical compositions were
445 determined from the STEM/EDS data using the Cliff-Lorimer equation[53]. We used the
446 composition of olivine grains obtained with the SEM/EDS as an internal standard for
447 determining Cliff-Lorimer k-factors.

448 Unpolarized infrared spectra of the recovered harzburgite samples were measured
449 using a JASCO IRT-5200EUO Fourier-transform infrared spectrometer (FTIR) with a
450 mid-infrared light source, a KBr beam splitter and a mercury cadmium telluride detector.
451 The doubly-polished thin sections with thickness of 40−90 μm were placed on a BaF_2
452 plate in dried air. An aperture size of 50×50 μm^2 was used for all of the measurements.
453 At least five spectra were obtained from each section with 128 integrated scans with 4
454 cm^{-1} resolution. The spectra were normalized by the thickness of the sections. The water

455 content in olivine was determined by integrating infrared absorption spectra from 3100
456 to 3750 cm^{-1} on the basis of the extinction coefficient calibration by Paterson[54] using an
457 orientation factor of 1/3 and the extinction coefficients for olivine.
458

References

1 Green II, H. W. Solving the paradox of deep earthquakes. *Sci Am* **271**, 64-71 (1994).

2 Green II, H. W. & Burnley, P. C. A new self-organizing mechanism for deep-focus earthquakes. *Nature* **341**, 733-737 (1989).

3 Schubnel, A. *et al.* Deep-focus earthquake analogs recorded at high pressure and temperature in the laboratory. *Science* **341**, 1377-1380 (2013).

4 Kirby, S. H., Durham, B. & Stern, L. A. Mantle phase changes and deep-earthquake faulting in subducting lithosphere. *Science* **252**, 216-225 (1991).

5 Green II, H. W., Shi, F., Bozhilov, K., Xia, G. & Reches, Z. Phase transformation and nanometric flow cause extreme weakening during fault slip. *Nat Geosci* **8**, 484-490 (2015).

6 Green II, H. W., Young, T. E., Walker, D. & Scholz, C. Z. Anticrack-associated faulting at very high pressure in natural olivine. *Nature* **348**, 720-722 (1990).

7 Officer, T. & Secco, R. A. Detection of high P, T transformational faulting in Fe_2SiO_4 via in-situ acoustic emission: Relevance to deep-focus earthquakes. *Phys Earth Planet Inter* **300**, 106429 (2020).

8 Aben, F. M. *et al.* Dynamic fracturing by successive coseismic loadings leads to pulverization in active fault zones. *J Geophys Res* **121**, 2338-2360, doi:10.1002/2015JB012542 (2015).

9 Kelemen, P. B. & Hirth, G. A periodic shear-heating mechanism for inteermediate-depth earthquakes in the mantle. *Nature* **446**, 787-790 (2007).

10 John, T. *et al.* Generation of intermediate-depth earthquakes by self-localizing thermal runaway. *Nature Geo* **2**, 137-140 (2009).

11 Kerschhofer, L., Sharp, T. G. & Rubie, D. C. Intracrystalline transformation of olivine to wadsleyite and ringwoodite under subduction zone conditions. *Science* **274**, 79–81 (1998).

12 Kawazoe, T., Karato, S., Otsuka, K., Jing, Z. & Mookherjee, M. Shear deformation of dry polycrystalline olivine under deep upper mantle conditions using a rotational Drickamer apparatus (RDA). *Phys. Earth Planet. Inter.* **174**, 128-137 (2009).

13 Evans, B. & Goetze, C. The temperature variation of hardness of olivine and its implication for polycrystalline yield stress. *J. Geophys. Res.* **84**, 5505-5524 (1979).

14 Raterron, P., Wu, Y., Weidner, D. J. & Chen, J. Low-temperature olivine rheology at high pressure. *Phys Earth Planet Inter* **145**, 149-159 (2004).

15 de Ronde, A. A., Dobson, D. P., Meredith, P. G. & Boon, S. A. Three-dimensional location and waveform analysis of microseismicity in multi-anvil experiments. *Geophys J Int* **171**, 1282-1294 (2007).

16 Kirby, S. H., Stein, S., Okal, E. A. & Rubie, D. C. in *Reviews of Geophysics* Vol. 34 261-306 (American Geophysical Union, 1996).

17 Asahara, Y., Ohtani, E. & Suzuki, A. Melting relations of hydrous and dry mantle compositions and the genesis of komatiites. *Geophys Res Lett* **25**, 2201-2204 (1998).

18 Takahashi, E. Melting of a dry peridotite KLB-1 up to 14 GPa: implications on the origin of peridotitic upper mantle. *J Geophys Res* **91**, 9367-9382 (1986).

501 19 Akaogi, M., Ito, E. & Navrotsky, A. Olivine-modified spinel-spinel transitions in the
502 system Mg_2SiO_4 - Fe_2SiO_4: calorimetric measurements, thermochemical calculation,
503 and geophysical application. *J Geophys Res* **94**, 15671-15685 (1989).
504 20 Ohtani, E. Melting relation of Fe_2SiO_4 up to about 200 kbar. *J phys Earth* **27**, 189-
505 208 (1979).
506 21 Healy, D., Jones, R. R. & Holdsworth, R. E. Three-dimensional brittle shear
507 fracturing by tensile crack interaction. *Nature* **439**, 64-67 (2006).
508 22 Lei, X., Kusunose, K., Rao, M. V. M. S., Nishizawa, O. & Satoh, T. Quasi-static fault
509 growth and cracking in homogeneous brittle rock under triaxial compression using
510 acoustic emission monitoring. *J Geophys Res* **105**, 6127-6139 (2000).
511 23 Däßler, R., Yuen, D. A., Karato, S. & Riedel, M. R. Two-dimensional thermo-kinetic
512 model for the olivine-spinel phase transition in subducting slabs. *Phys Earth Planet*
513 *Inter* **94**, 217-239 (1996).
514 24 Kanamori, H., Anderson, D. L. & Heaton, T. H. Frictional melting during the
515 rupture of the 1994 Bolivian earthquake. *Science* **279**, 839-842 (1998).
516 25 Karato, S. *Deformation of Earth materials: An introduction to the rheology of solid*
517 *Earth*. (Cambridge Univ Press, 2008).
518 26 Abramson, E. H., Browon, J. M., Slutsky, L. J. & Zaug, J. The elastic constants of
519 San Carlos olivine up to 17 GPa. *J. Geophys. Res.* **105**, 7893–7908 (1997).
520 27 Webb, S. L. The elasticity of the Upper mantle orthosilicates olivine and garnet to 3
521 GPa. *Phys Chem Min* **16**, 684-692 (1989).

28 Xu, Y. *et al.* Thermal diffusivity and conductivity of olivine, wadsleyite and ringwoodite to 20 GPa and 1373 K. *Phys Earth Planet Inter* **143-144**, 321-336 (2004).

29 Hirth, G. & Kohlstedt, D. L. in *Inside the subduction factory* Vol. Geophys. Monogr. Ser. (ed J Eiler) 83-105 (American Geophysical Union, 2003).

30 Shimojuku, A., Kubo, T., Ohtani, E., Nakamura, T. & Okazaki, R. Effects of hydroten and iron on the silicon diffusivity of wadsleyite. *Phys Earth Planet Inter* **183**, 175-182 (2010).

31 Karato, S., Riedel, M. R. & Yuen, D. A. Rheological structure and deformation of subducted slabs in the mantle transition zone: implications for mantle circulation and deep earthquakes. *Phys Earth Planet Inter* **127**, 83-108 (2001).

32 Schubert, G., Yuen, D. A. & Turcotte, D. L. Role of phase transitions in a dynamic mantle. *Geophys J R Astr Soc* **42**, 705-735 (1975).

33 Bina, C. R. A note on latent heat release from disequilibrium phase transformations and deep seismogenesis. *Earth Planet Space* **50**, 1029-1034 (1998).

34 Guest, A., Schubert, G. & Gable, C. W. Stresses along the metastable wedge of olivine in a subducting slab: possible explanation for the Tonga double seismic layer. *Phys Earth Planet Inter* **141**, 253-267 (2004).

35 Billen, M. Deep slab seismicity limited by rate of deformation in the transition zone. *Science Advances* **6**, eaaz7692 (2020).

36 Shimojuku, A. *et al.* Si and O diffusion in $(Mg,Fe)_2SiO_4$ wadsleyite and ringwoodite

and its implications for the rheology of the mantle transition zone. *Earth Planet Sci Lett* **284**, 103-112 (2009).

37 Kawakatsu, H. & Yoshioka, S. Metastable olivine wedge and deep dry cold slab beneath sowthwest Japa. *Earth Planet Sci Lett* **303**, 1-10 (2011).

38 Jiang, G., Zhao, D. & Zhang, G. Detection of metastable olivine wedge in the western Pacific slab and its geodynamic implications. *Phys Earth Planet Inter* **238**, 1-7 (2015).

39 Wiens, D. A., McGuire, J. J. & Shore, P. J. Evidence for transformational faulting from a deep double seismic zone in Tonga. *Nature* **264**, 790-793 (1993).

40 Wiens, D. A. & Gillbert, H. J. Effect of slab temperature on deep-earthquake aftershock productivity and magnitude-frequency relations. *Nature* **384**, 153-156 (1996).

41 Zhan, Z. Gutenberg-Richter law for deep earthquakes revisited: A dual-mechanism hypothesis. *Earth Planet Sci Lett* **461**, 1-7 (2017).

42 Kubo, T., Kaneshima, S., Torii, Y. & Yoshioka, S. Seismological and experimental constraints on metastable phase transformations and rheology of the Mariana slab. *Earth Planet Sci Lett* **287**, 12-23 (2009).

43 Frohlich, C. The nature of deep-focus earthquakes. *Ann Rev Earth Planet Sci* **17**, 227-254 (1989).

44 Ohuchi, T. *et al.* Dislocation-accommodated grain boundary sliding of water-rich olivine in the Earth's deep upper mantle. *Science Advances* **1**, e1500360,

564 doi:10.1126/sciadv.1500360 (2015).

565 45 Ohuchi, T. *et al.* Intermediate-depth earthquakes linked to localized heating in
566 dunite and harzburgite. *Nat Geosci* **10**, 771-776, doi:10.1038/ngeo3011 (2017).

567 46 Handy, M. R. The solid-state flow of polymineralic rocks. *J Geophys Res* **95**, 8647-
568 8661 (1990).

569 47 Kanzaki, M. Crystal structure of a new high-pressure polymorph of topaz-OH. *Am.*
570 *Mineral.* **95**, 1349–1352 (2010).

571 48 Liu, W., Kung, J. & Li, B. Elasticity of San Carlos olivine to 8 GPa and 1073 K.
572 *Geophys. Res. Lett.* **32**, L16301, doi:10.1029/2005GL023453 (2005).

573 49 Singh, A. K., Balasingh, C., Mao, H.-K., Hemley, R. J. & Shu, J. Analysis of lattice
574 strains measured under nonhydrostatic pressure. *J. Appl. Phys.* **83**, 7567-7575
575 (1998).

576 50 Isaak, D. G. High-temperature elasticity of iron-bearing olivines. *J. Geophys. Res.*
577 **97**, 1871–1885 (1992).

578 51 Akaike, H. in *2nd International symposium on information theory* (eds B Petrov
579 & F Csaki) 267-281 (Budapest Akademiai Kiado, 1973).

580 52 Lei, X. in *Fractal analysis for natural hazards* Vol. 261 (ed G & Malamud Cello, B
581 D) 11-29 (The Geological Society of London, 2006).

582 53 Cliff, G. & Lorimer, G. The quantitative analysis of thin specimens. *J Microsc* **103**,
583 203-207 (1975).

584 54 Paterson, M. S. The determination of hydroxyl by infrared absorption in quartz,

585 silicate glasses and similar materials. *Bull. Minéral.* **105**, 20–29 (1982).

586

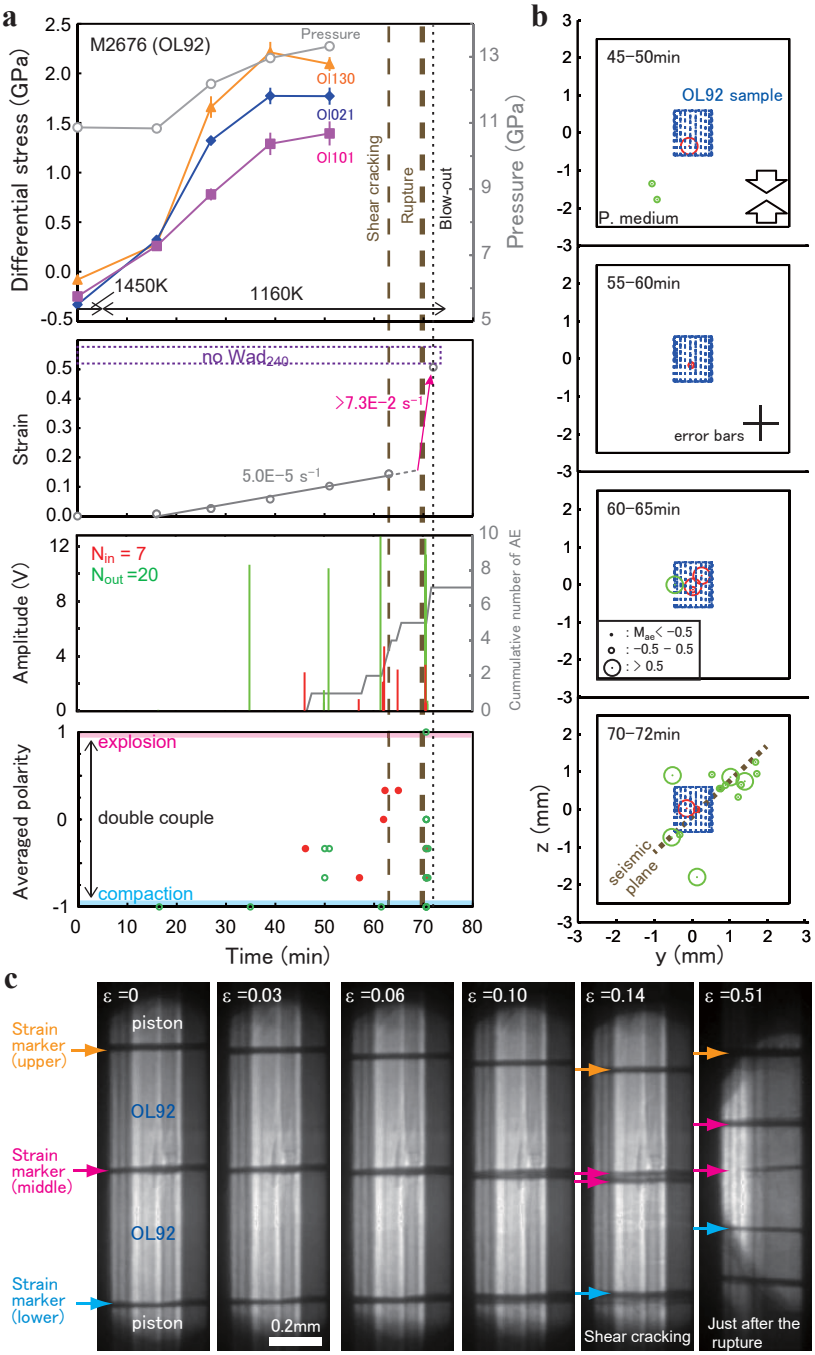

Figure 1 | Mechanical and acoustic records in the OL92 sample faulted at 1160 K (M2676). a, The stress values were obtained from three diffraction peaks of olivine (diamond: 021, square: 101, triangle: 130). Pressure and strain are shown by gray open circles. The cumulative number of AEs (gray line), amplitudes (red impulses: AEs from the inside of the sample; green: outside of the sample), and the average of polarity values are plotted against time. The total number of AE events (N_{in}: from the inside of the sample: N_{out}: outside of the sample) is also shown. The timings of shear cracking, rupture, and blow-out are shown by thin-dashed, thick-dashed and dotted lines, respectively. **b**, Two-dimensional views of AE hypocenters in the deforming sample (blue cylinder) and the pressure medium (black square) during periods of each 5 (or 2) minutes. The black cross shows typical errors for the location of hypocenter. A brown-dashed line shows the seismic plane observed at the timing of rupture. Arrows represent the compressional direction. **c**, X-ray radiographs of the deforming sample at each strain ε. Positions of platinum strain markers are shown by arrows. Splitting of the middle strain marker (ε =0.14 at 62 min) suggests shear cracking followed by faulting. Direction of the incident X-ray is perpendicular to the radiograph images.

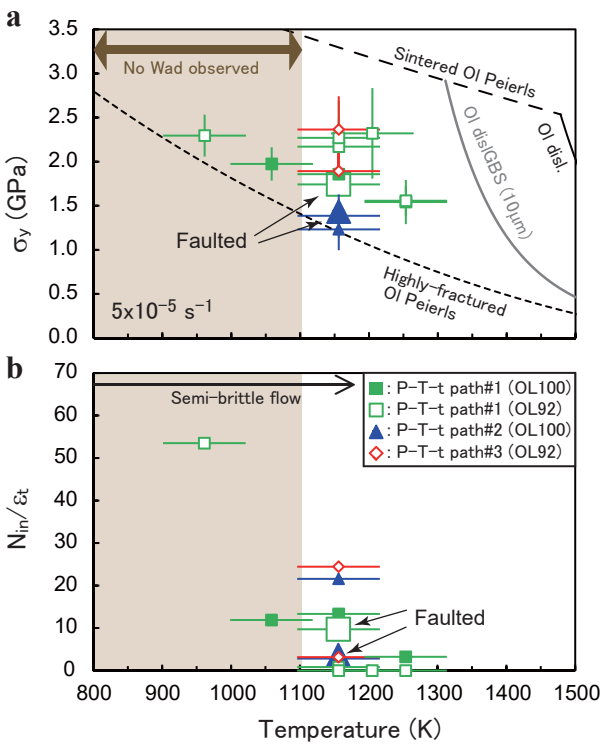

Figure 2 | Summary of yield strength (σ_y) and averaged AE rate (N_{in}/ε_t). a, Temperature dependence of σ_y of the samples (solid: OL100, open: OL92). Large symbols represent the samples with faulting (M2676 and M3100). Creep strength of olivine (Ol) is calculated assuming the Peierls creep (for sintered aggregates[8,13]; highly-fractured powdered samples[14]), wet dislocation (disl.) creep[29]; wet dislocation-accommodated grain boundary sliding (dislGBS; for a typical grain size of 10 μm)[44]. The brown area represents the range of temperatures at which no nucleation of wadsleyite was observed in the recovered samples. **b**, Temperature dependence of N_{in}/ε_t, where N_{in} is the total number of AE events in the sample and ε_t is the total strain.

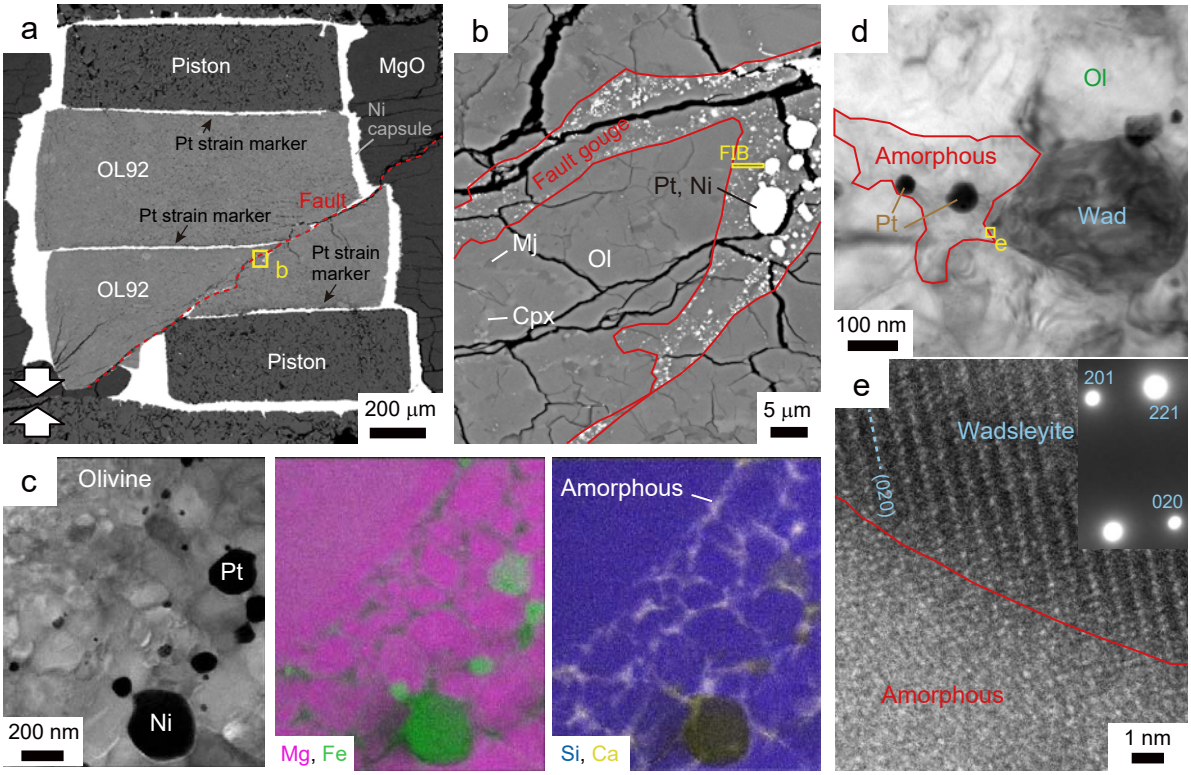

Figure 3 | Microstructures of the OL92 sample faulted at 1160 K (M2676). a, A secondary electron image of the recovered sample. The fault is highlighted by a red dashed line. **b**, A magnified image of the fault (yellow square in a). **c**, A STEM image and element maps showing the gouge layer in the fault. In the element maps, grayscale corresponds to concentration of elements (pink: magnesium; green: iron; blue: silicon; yellow: calcium). Platinum (Pt) and nickel (Ni) blobs are distributed along the network of the amorphous phase. The FIB foil was prepared from the area shown in b (yellow square). **d**, A TEM image of a wadsleyite (Wad) next to an amorphous pocket in the fault gouge. **e**, A high-resolution TEM image showing the boundary between the wadsleyite grain and the amorphous pocket.

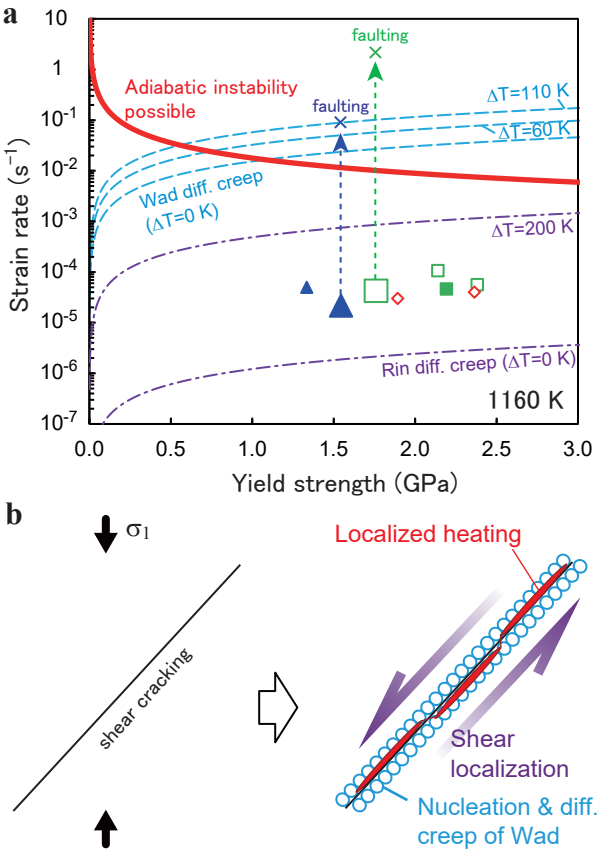

Figure 4 | Occurrence of transformational faulting under conditions of the mantle transition zone. a, Conditions for localized heating in metastable olivine at pressures of 13−15.5 GPa and the background temperature of 1160 K. The thick-solid curve shows the critical strain rate for the adiabatic instability, where deformation of the wall rock is controlled by the Peierls creep[12,13]. Long-dashed curves represent the creep strength of ultrafine-grained wadsleyite (grain size of 20 nm) without (ΔT =0 K) and with (=60 K at 13 GPa; 110 K at 15.5 GPa) the effect of superheating (Eq. 2). Dot-dashed curves are the corresponding estimates for ringwoodite. Our experimental results at 1160 K are shown by symbols. Crosses show the estimated strain rate at the timing of faulting (see text). **b**, Schematic illustration of the present transformational faulting model. At the temperatures of ~1160K, shear cracking is followed by a rapid nucleation of nano-crystalline wadsleyite on the crack surface. Diffusion creep of such fine-grained wadsleyite induces shear localization associating localized heating.

Supplementary Information to "Deep seismic faulting triggered by nano-crystallization of wadsleyite from olivine"

T. Ohuchi, Y. Higo, Y. Tange, T. Sakai, and T. Irifune

1. Kinetics of the olivine-wadsleyite phase transformation

To estimate the rate of olivine-wadsleyite phase transformation on crack surfaces under our experimental conditions, we adopt theoretical equations for the kinetics of polymorphic phase transformations on interfaces. The nucleation rate $\dot{N}$ and growth rate $\dot{x}$ during the early stages of phase transformation follows[1,2]:

$$\dot{N} = a_0 T exp\left(-\frac{\phi \Delta G^*_{hom}}{kT}\right) exp\left(-\frac{Q}{RT}\right) \quad \text{(S1)}$$

$$\dot{x} = b_0 T exp\left(\frac{Q}{RT}\right)\left[1 - exp\left(-\frac{\Delta G_r}{RT}\right)\right] \quad \text{(S2)}$$

where a_0 and b_0 are constants, ϕ is a shape factor, ΔG^*_{hom} is the activation energy for homogeneous nucleation, ΔG_r is the free energy change of reaction, Q is the activation energy for growth, k is the Boltzmann constant, and R is the molar gas constant. We adopt Q =404 kJ/mol for the olivine-wadsleyite transformation[3] and $k_0 = 5.3 \times 10^{42}$ $s^{-1}m^{-2}K^{-1}$ for the Ni_2SiO_4 α-γ transformation[1]. Reported values of $\phi = 6 \times 10^{-4}$ and 1×10^{-4}

were used for nucleation of wadsleyite on grain boundaries and crack surfaces, respectively[1,4]. The values of ΔG^*_{hom} and ΔG_r were calculated from the thermodynamic data of the olivine-wadsleyite transformation[5] and the olivine-wadsleyite phase boundary[6]. The kinetics of the volume fraction transformed are described as the Avrami equation and the rate constant during the early stages of transformation k is given as[1]:

$$\mathrm{k} = \frac{\pi}{3}\dot{N}\dot{x}^3 \qquad \text{(S3)}$$

Formation of the ultrafine-grained gouge on crack surfaces is effective when both $\dot{N}$ and k are high. The temperature dependences of the parameters are shown in Extended Data Fig. 7. See main text for further discussion.

References

1 Rubie, D. C. *et al.* An in situ X ray diffraction study of the kinetics of the Ni_2SiO_4 olivine-spinel transformation. *J. Geophys. Res.* **95**, 15829-15844 (1990).

2 Dowty, E. in *Physics of magmatic processes* (ed R B Hargravers) 419-485 (Princeton University Press, 1980).

3 Mosenfelder, J. L., Marton, F. C., Ross II, C. R., Kerschhofer, L. & Rubie, D. C. Experimental constraints on the depth of olivine metastability in subducting lithosphere. *Phys. Earth Planet. Inter.* **127**, 165-180 (2001).

4 Däßler, R., Yuen, D. A., Karato, S. & Riedel, M. R. Two-dimensional thermo-kinetic model for the olivine-spinel phase transition in subducting slabs. *Phys. Earth Planet. Inter.* **94**, 217-239 (1996).

5 Akaogi, M., Ito, E. & Navrotsky, A. Olivine-modified spinel-spinel transitions in the system Mg_2SiO_4 - Fe_2SiO_4: calorimetric measurements, thermochemical calculation, and geophysical application. *J. Geophys. Res.* **94**, 15671-15685 (1989).

6 Kerschhofer, L., Sharp, T. G. & Rubie, D. C. Intracrystalline transformation of olivine to wadsleyite and ringwoodite under subduction zone conditions. *Science* **274**, 79–81 (1998).

7 Takahashi, E. Melting of a dry peridotite KLB-1 up to 14 GPa: implications on the origin of peridotitic upper mantle. *J. Geophys. Res.* **91**, 9367-9382 (1986).

8 Ohtani, E. Melting relation of Fe_2SiO_4 up to about 200 kbar. *J. Phys. Earth* **27**, 189-208 (1979).

9 Ohuchi, T. *et al.* Intermediate-depth earthquakes linked to localized heating in dunite and harzburgite. *Nat. Geosci.* **10**, 771-776, doi:10.1038/ngeo3011 (2017).

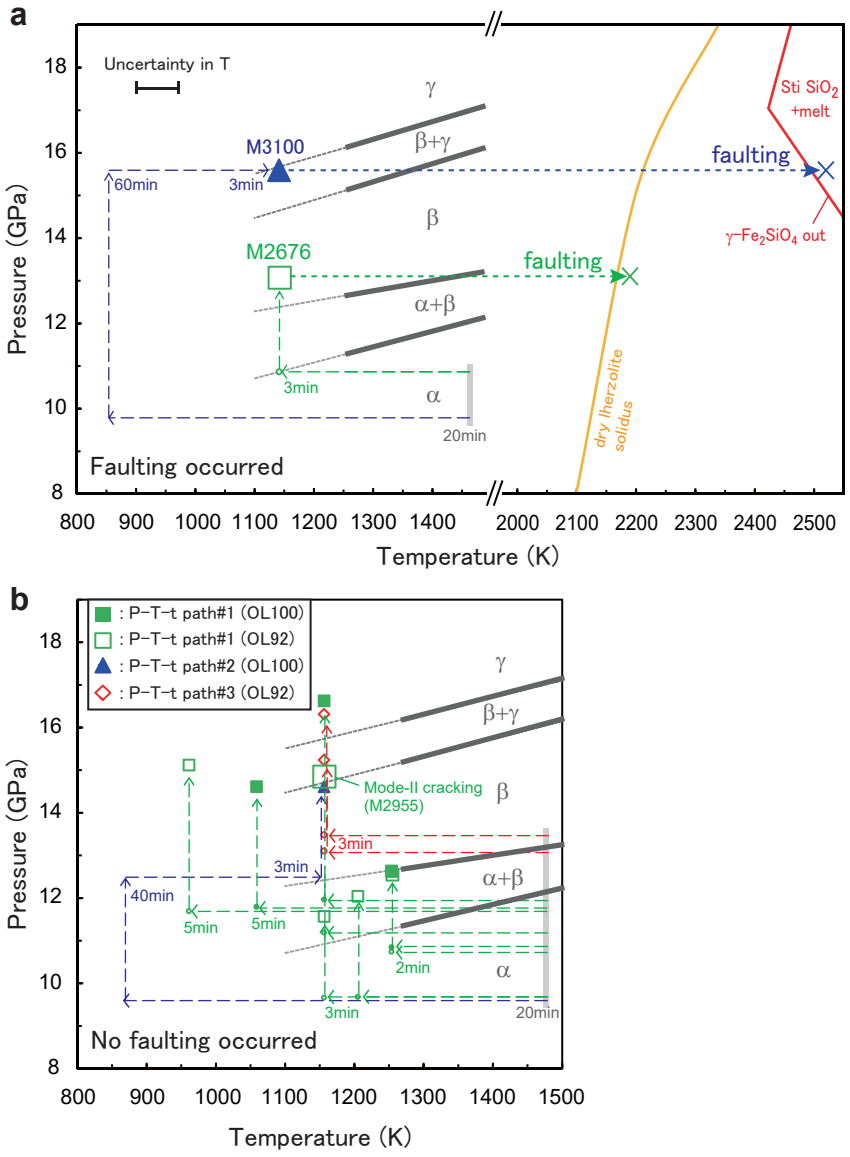

Extended Data Figure 1 | Summary of experimental conditions as a function of pressure, temperature, and time. a, Faulting occurred. **b,** No faulting occurred. The dashed arrows indicate the P-T-t paths for our experiments. Numbers refer to the durations of the stages of annealing (20 min), temperature decrease/increase (2−5 min), and pressure increase (40−60 min) before the deformation stage. Square, triangle, and diamond represent the P-T-t path#1 (normal), #2 (overpressurized just before the deformation), and #3 (annealing in the wadsleyite-stability field before the deformation), respectively. Solid and open symbols represent the runs in which the OL100 and OL92 samples were used, respectively. The equilibrium boundaries of α (olivine), β (wadsleyite), and γ (ringwoodite) for $Mg_{1.8}Fe_{0.2}SiO_4$ are shown by gray solid lines (Kerschhofer et al. [6]). In a, partial melting of the OL92 sample is possible above the solidus curve (orange) for dry lherzolite (Takahashi [7]). Note that the conditions for incongruent melting of γ-Fe_2SiO_4 to a liquid phase and stishovite (Sti) for fayalite (Ohtani [8]) shown by the red line gives the lower limit of the melting temperature of β/γ-$Mg_{1.8}Fe_{0.2}SiO_4$. In b, the P-T condition for deformation of the M2955 sample, in which a mode-II throughgoing crack occurred, is highlighted by a large symbol.

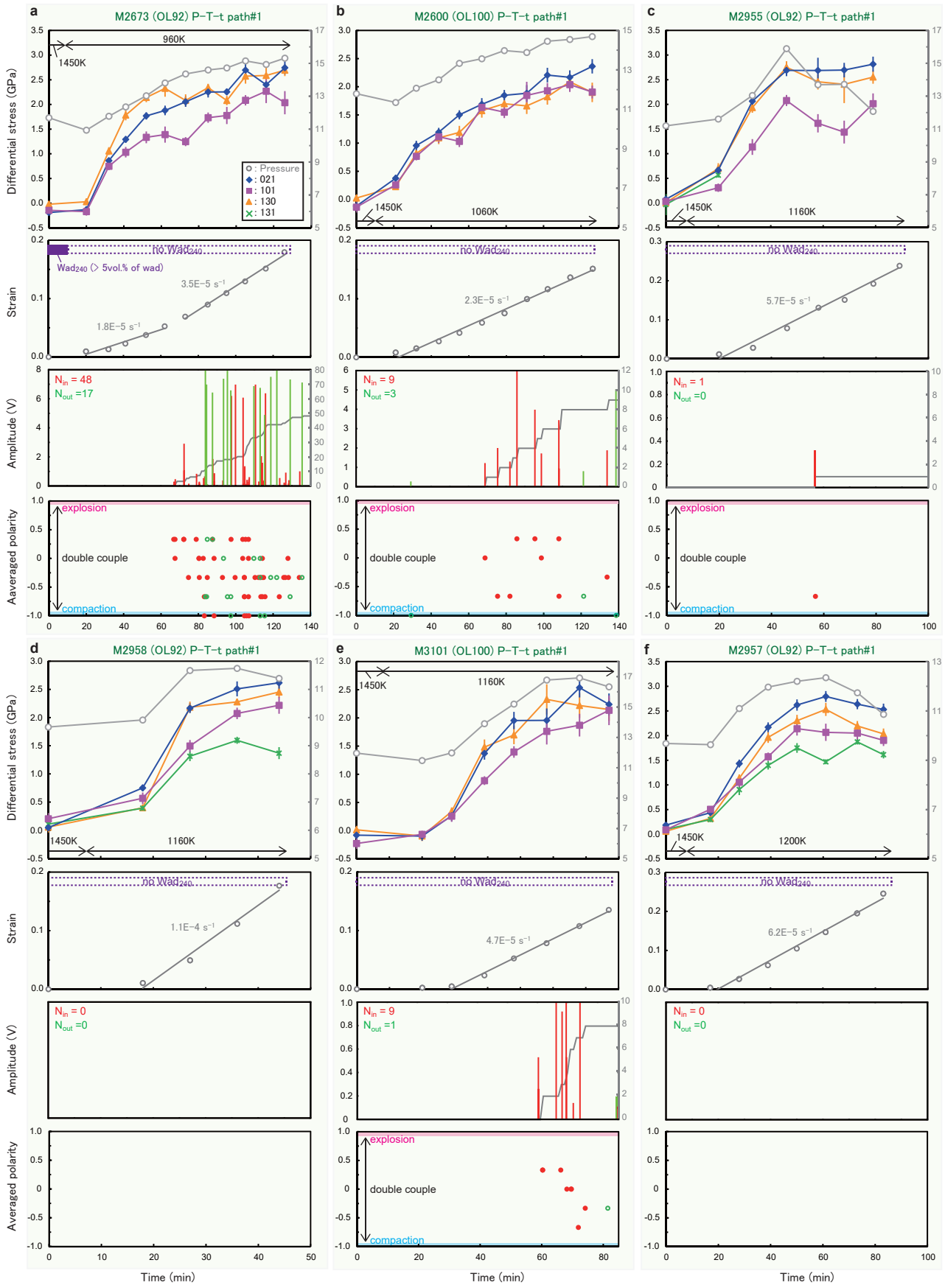

Extended Data Figure 2 | Mechanical and acoustic records plotted against time during the deformation stage. The stress values were obtained from four diffraction peaks of olivine (solid diamond: 021, solid square: 101, solid triangle: 130, cross: 131). The duration in which wadsleyite 240 (Wad_{240}) peak was detected is highlighted by the thick purple line. Other symbols, lines, and abbreviations have the same meanings as shown in Fig. 1a. The average of polarity values, which were obtained from the first motions of six waveforms, equals to 1 and -1 in the cases of isotropic volume increase (i.e., explosion) and decrease (i.e., compaction), respectively. Double couple source is expected when the absolute value of polarity is less than 1 (i.e., both positive and negative polarities are detected in an AE event).

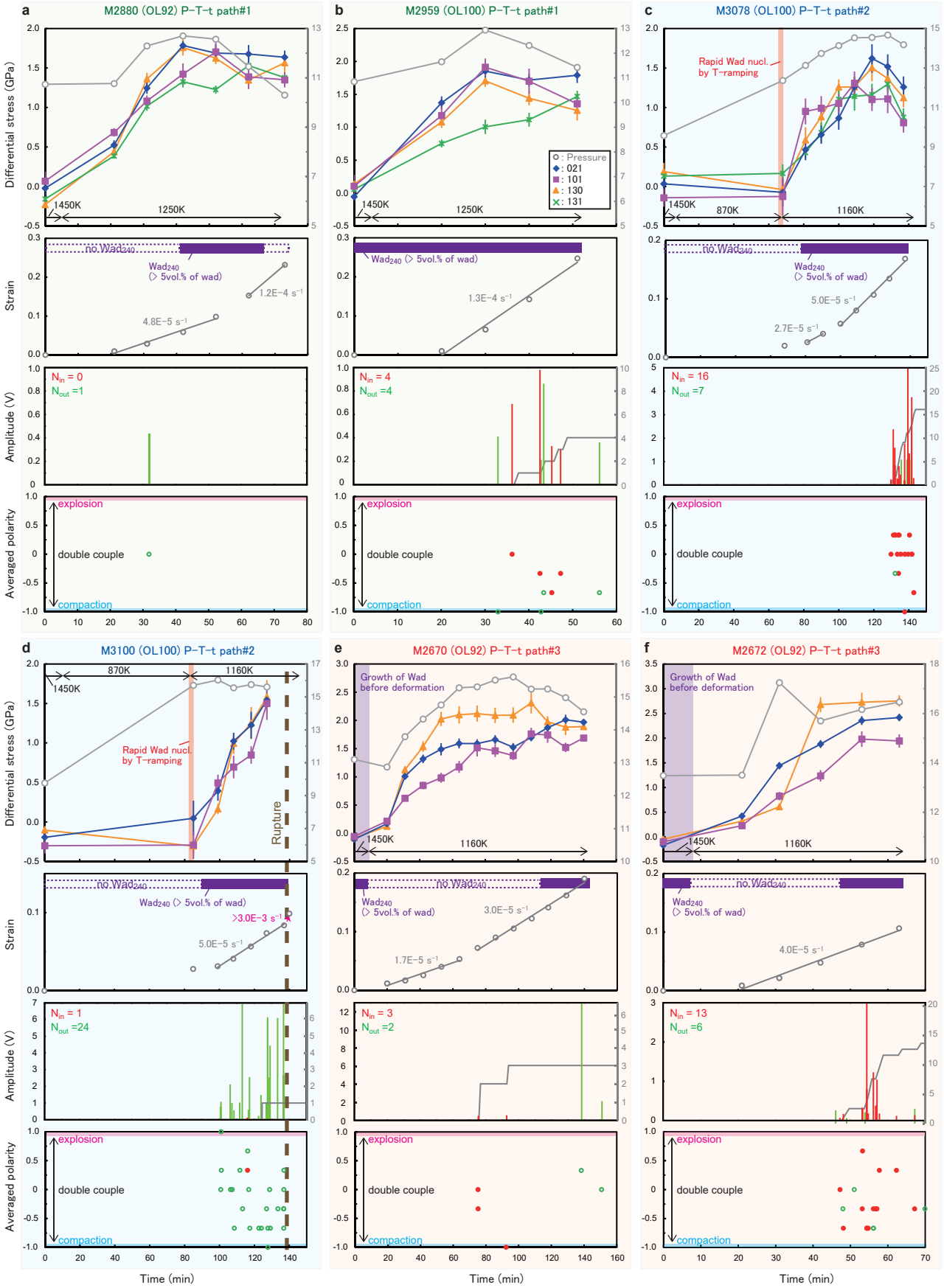

Extended Data Figure 3 | Mechanical and acoustic records plotted against time during the deformation stage (continued). Symbols, lines, and abbreviations have the same meanings as shown in Extended Data Fig. 2. The pale-red area in the stress-time diagram shows the timing of rapid nucleation of wadsleyite due to temperature ramping in the P-T-t path#2. The pale-purple area in the stress-time diagram represents the duration of the annealing stage in which growth of wadsleyite proceeded in the path#3.

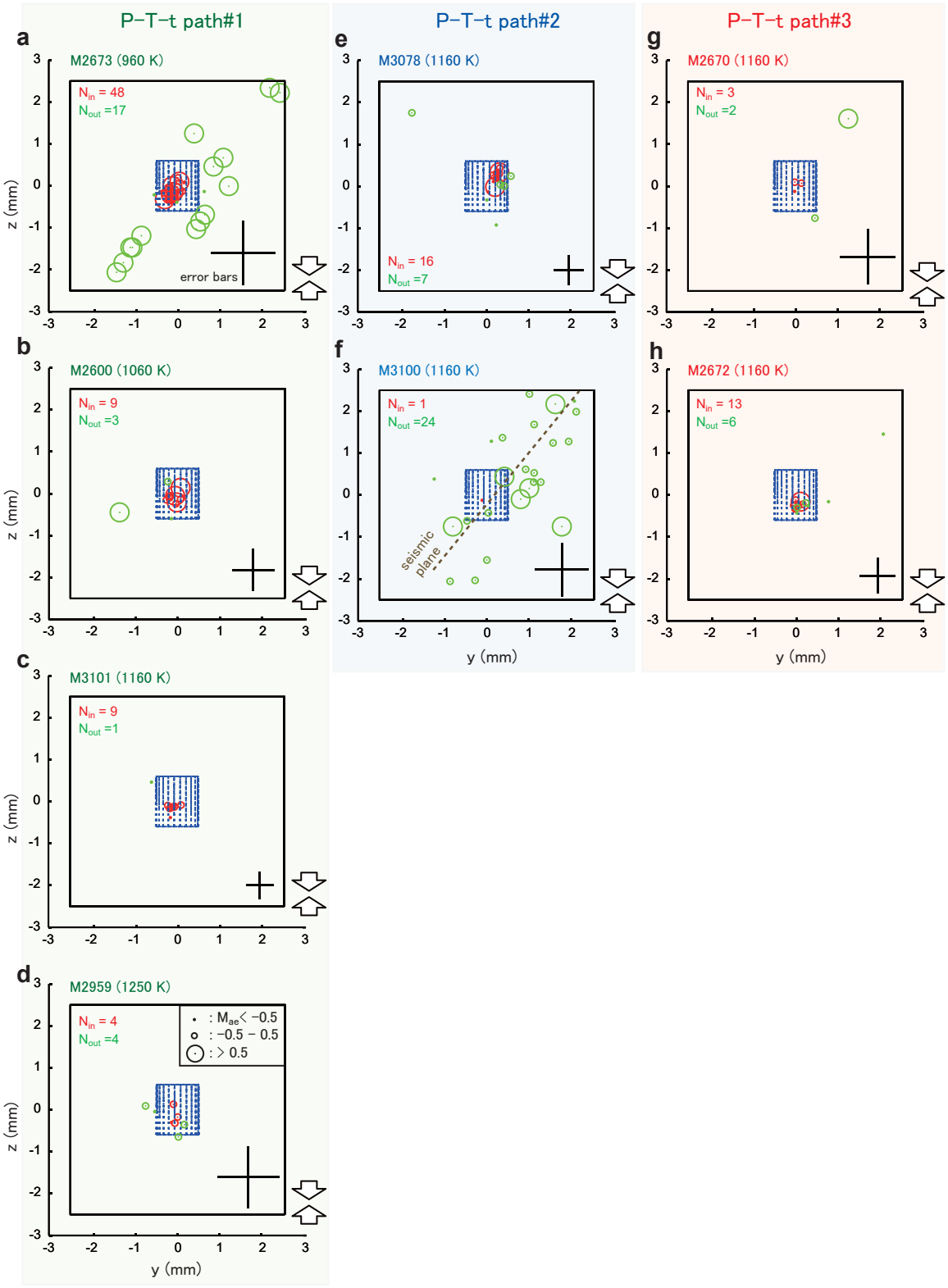

Extended Data Figure 4 | Two-dimensional views of AE hypocentres in deforming samples. **a-d**, Hypocentres in the samples deformed at 960−1250 K via the P-T-t path#1. **e-f**, Hypocentres in the samples deformed at 1160 K via the P-T-t path#2. **g-h,** via the P-T-t path#3. Symbols, lines, arrows and abbreviations have the same meanings as shown in Fig. 1b.

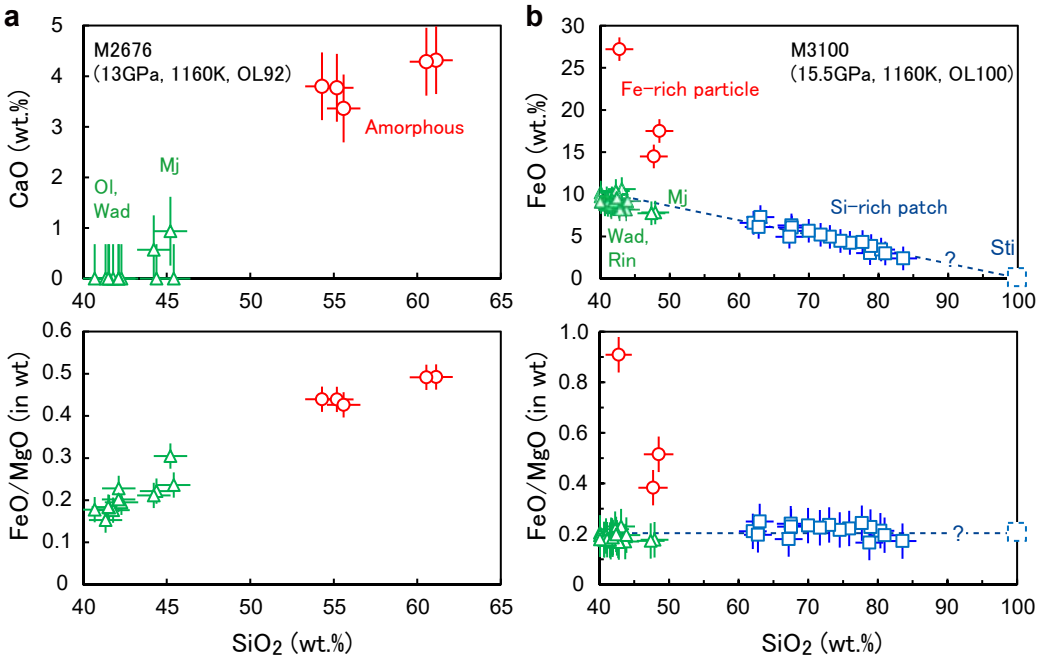

Extended Data Figure 5 | Chemical compositions of the phases obtained with a STEM/EDS (in wt.%). a, Chemical compositions of olivine/wadsleyite (Ol, Wad: triangles), majorite (triangles), and amorphous phase (circle) in the fault gouge observed in the M2676 sample. **b**, Chemical compositions of wadsleyite/ringwoodite (Wad, Rin: triangles), majorite (triangles), silicon-rich patches (Si-rich: squares), and iron-rich particles (Fe-rich: circles) in the damage zone developed in the M3100 sample. The dashed line is the mixing line between wadsleyite (or ringwoodite) and stishovoite (Sti) expected from the variation in SiO_2 concentration in the silicon-rich patches. Chemical compositions are recalculated as 100 wt.% anhydrous.

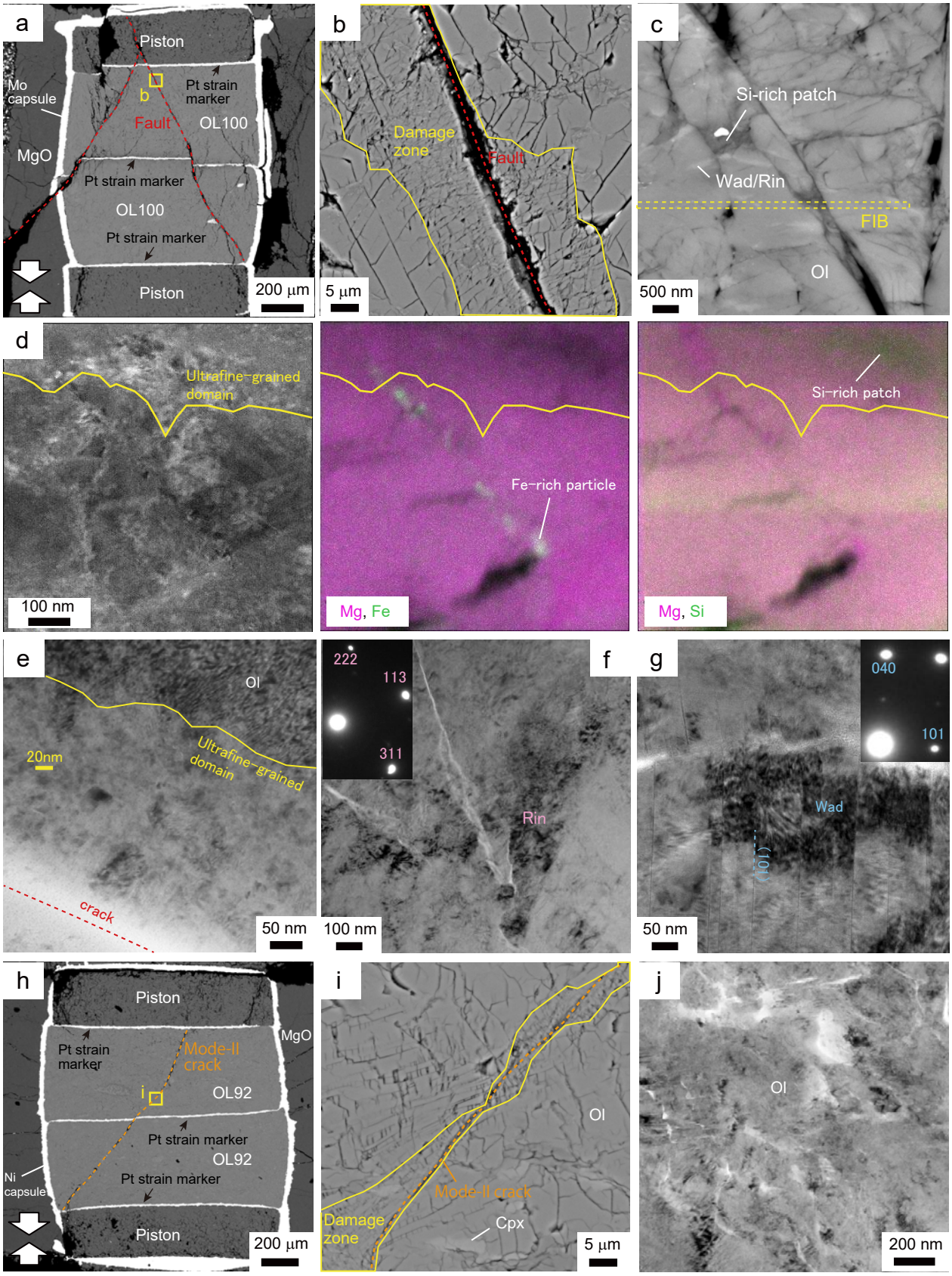

Extended Data Figure 6 | Microstructures in the faulted/fractured samples. a, A backscattered electron image of an OL100 sample faulted at 1160 K (M3100). Faults are highlighted by red-dashed lines. **b**, A magnified view of a fault associating a damage zone (the region "b" in a). **c**, A close-up of the damage zone. Middle gray: olivine (Ol); light gray: wadsleyite (Wad) or ringwoodite (Rin); dark gray: silicon-rich patch. **d**, A STEM image and element maps showing the damage zone. In element maps, grayscale corresponds to concentration of elements (pink: magnesium; green: iron or silicon). The FIB foil was prepared from the area shown in c (yellow square). **e**, A TEM image of an ultrafine-grained domain in the damage zone. Typical grain size is ~20 nm. **f-g**, TEM micrographs of a ringwoodite and a wadsleyite grains in the damage zone. Diffraction patterns are also shown. The wadsleyite grain is cleavaged on the (101) plane. **h**, A backscattered electron image of an OL92 sample fractured at 1160 K (M2955). A mode-II crack (i.e., shear crack) is highlighted by the orange-dashed line. **i**, A magnified view of the mode-II crack (the region "i" in h). A damage zone is developed around the crack. **j**, A TEM image of the damage zone. High-pressure phases of olivine are not observed.

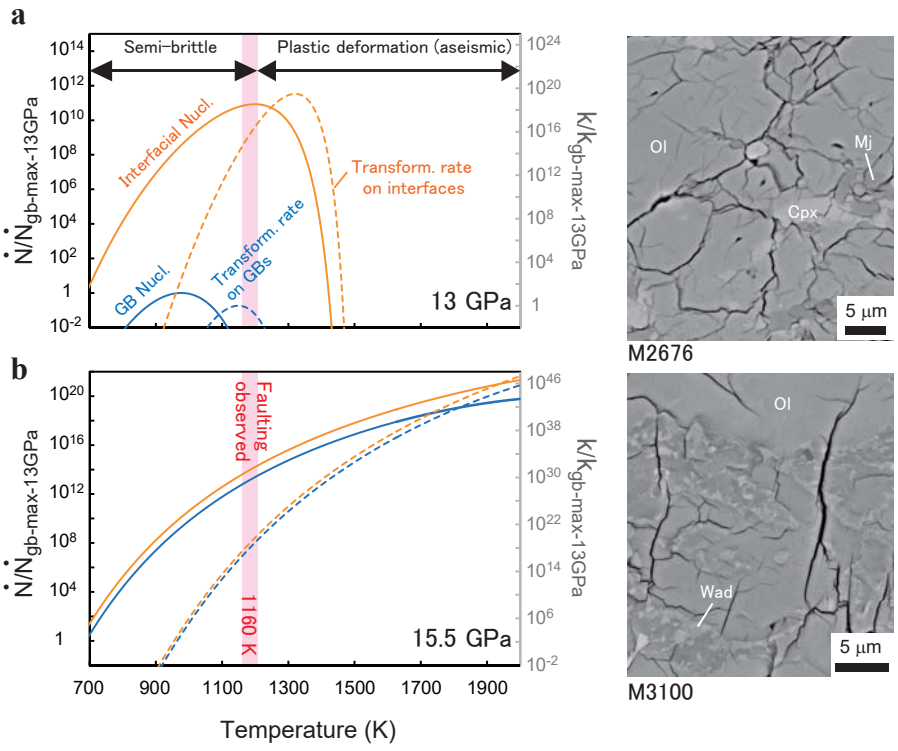

Extended Data Figure 7 | Numerical model results for nucleation of wadsleyite. a, At 13 GPa. **b**, At 15.5 GPa. The temperature dependence of the wadsleyite nucleation rate $\dot{N}$ (solid curves) and the rate constant for the olivine-wadsleyite transformation k (dashed curves) are calculated from Eqs. (S1) and (S3), respectively. We considered two cases for the calculations: reactions on grain boundaries (GBs: blue) and on interfaces (orange). Shape factors (ϕ) for GB nucleation and interfacial nucleation are assumed as 6×10^{-4} and 1×10^{-4}, respectively. The values of $\dot{N}$ and k are normalized by their maximum values of the GB case at 13 GPa (i.e., $\dot{N}_{gb\text{-}max\text{-}13GPa}$ and $k_{gb\text{-}max\text{-}13GPa}$). The olivine-wadsleyite transformation is so sluggish that no wadsleyite grain was expected on olivine GBs, as observed in the M2676 sample. Numerous wadsleyite grains on olivine GBs in the M3100 sample are explained by the elevated transformation rate on GBs at 15.5 GPa. Semi-brittle flow associating AEs controls the sample shortening at temperatures below 1200 K. On the other hand, aseismic plastic deformation is dominant at higher temperatures. Faulting can proceed only when both microcracking and fast transition of olivine-wadsleyite transformation are possible at temperatures ~1160 K (pale-red area).

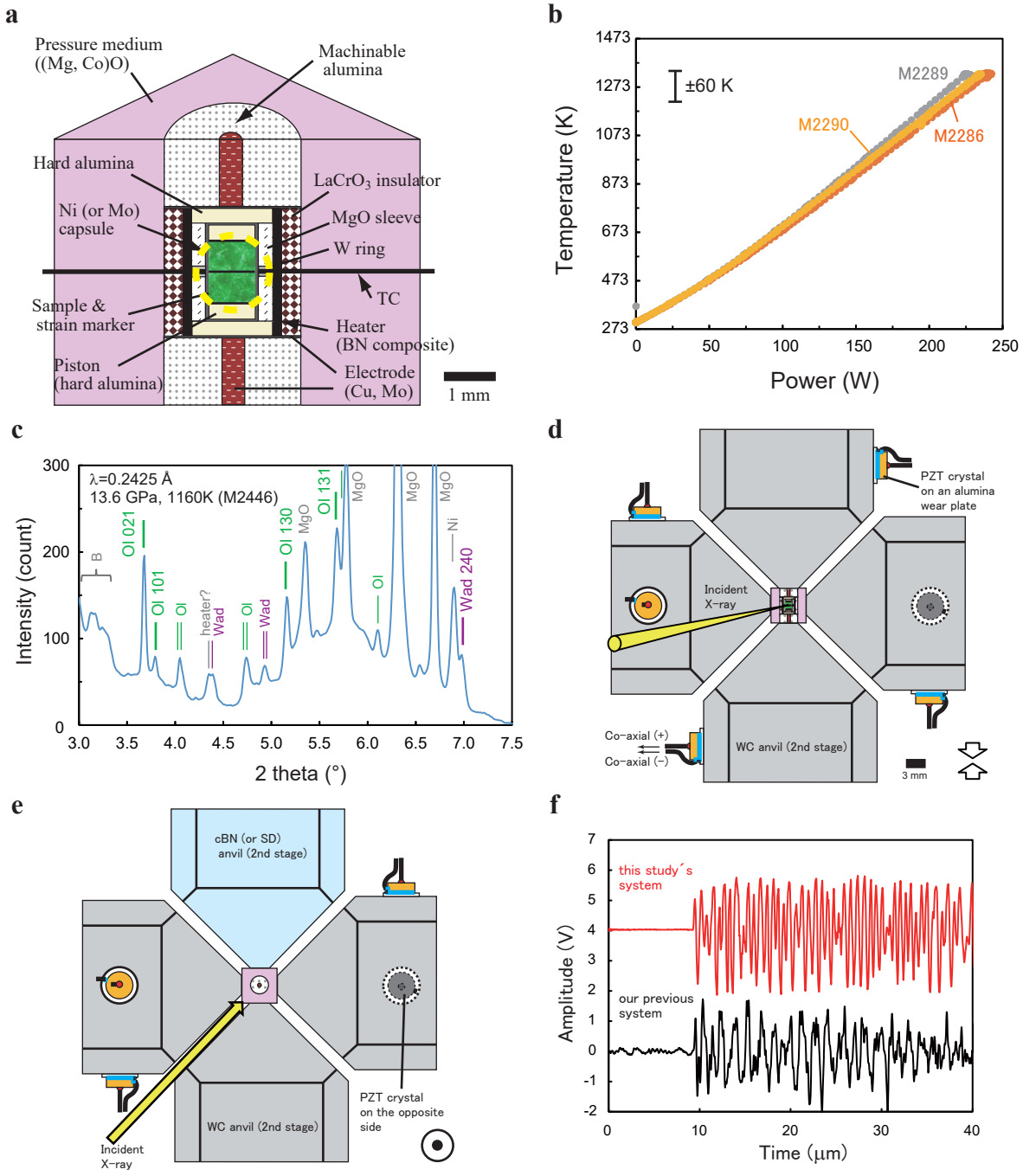

Extended Data Figure 8 | Experimental setup. a, The cell assembly viewed in cross section from the direction parallel to the X-ray path (dashed yellow circle). Note that the tungsten (W) rings and the thermocouple wires (TC) were not used for the deformation runs. **b**, Calibration of central temperature in the cell vs. furnace power under 0.6 MN main-ram load (corresponding to ~13 GPa at 1250 K). The three calibration runs (M2286, M2296, and M2290) were conducted at the BL04B1 beamline, SPring-8. **c**, A one-dimensional diffraction pattern integrated from a half ring of the two-dimensional diffraction pattern taken at 13.6 GPa and 1160 K (M2446). Diffraction patterns of olivine (Ol), wadsleyite (Wad), the MgO sleeve, a nickel capsule (Ni) are observed. **d-e**, Schematic representation of the experimental setup showing the positions of six PZT crystals (i.e., transducers) mounted on the sidewall surface of 2nd-stage anvils. Views from the directions perpendicular (d) and parallel (e) to the compressional direction. **f**, Sample waveforms of an AE radiated from an OL100 sample deformed at ~15 GPa and 1160 K (M2446). The AE event was monitored by two transducers: one was connected to a low-noise 30 dB pre-amplifier via an ultra-small pre-amplifiers (20 dB gain) (this study), and the other was connected to a low-noise 40 dB pre-amplifier used in our previous studies (Ohuchi et al. [9]).

Extended Table 1. Experimental conditions and results.

Run No.	Starting sample	P (GPa) [a]	T (K) [b]	Total strain	Strain rate (s^{-1}) [c]	$\sigma_{y,\ 021}$ (GPa) [d]	$\sigma_{y,\ 101}$ (GPa) [d]	$\sigma_{y,\ 130}$ (GPa) [d]	$\sigma_{y,\ 131}$ (GPa) [d]	Phase assemblage [e]	C_{OH} (wt. ppm) [f]	N_{in} [g]	N_{out} [g]	Formation of faults/cracks
P-T-t path#1														
M2673	OL92	15.1	960	0.18	3.5×10^{-5}	2.57 (± 0.10)	2.15 (± 0.24)	2.64 (± 0.14)	——	Ol + Mj + Cpx	150 (± 30)	48	17	No
M2600	OL100	14.6	1060	0.15	2.3×10^{-5}	2.27 (± 0.13)	1.97 (± 0.12)	1.99 (± 0.15)	——	Ol	10 (± 10)	9	3	No
M2676 [h]	OL92	13.1	1160	0.14	5.0×10^{-5}	1.77 (± 0.08)	1.34 (± 0.12)	2.15 (± 0.09)	——	Ol + Mj + Cpx + Wad + Amorphous	130 (± 20)	7	20	Fault
M2955	OL92	14.8	1160	0.24	5.7×10^{-5}	2.69 (± 0.15)	1.85 (± 0.13)	2.61 (± 0.19)	——	Ol + Mj + Cpx	170 (± 10)	1	0	Mode-II throughgoing crack
M2958	OL92	11.6	1160	0.18	1.1×10^{-4}	2.56 (± 0.13)	2.14 (± 0.13)	2.37 (± 0.08)	1.48 (± 0.08)	Ol + Mj + Cpx	320 (± 20)	0	0	No
M3101	OL100	16.6	1160	0.14	5.7×10^{-5}	2.39 (± 0.15)	2.00 (± 0.21)	2.18 (± 0.19)	——	Ol + Wad	50 (± 10)	9	1	No
M2957	OL92	12.0	1200	0.25	6.2×10^{-5}	2.72 (± 0.11)	2.06 (± 0.15)	2.36 (± 0.10)	1.67 (± 0.05)	Ol + Mj + Cpx	420 (± 10)	0	0	No
M2880	OL92	12.6	1250	0.23	1.2×10^{-4}	1.74 (± 0.08)	1.56 (± 0.13)	1.69 (± 0.09)	1.28 (± 0.06)	Ol + Mj + Cpx + Wad	—— [i]	0	1	No
M2959	OL100	12.6	1250	0.25	1.3×10^{-4}	1.78 (± 0.11)	1.81 (± 0.16)	1.57 (± 0.10)	1.06 (± 0.11)	Ol + Wad	140 (± 10)	4	4	No
P-T-t path#2														
M3078	OL100	14.6	1160	0.15	5.0×10^{-5}	1.57 (± 0.16)	1.11 (± 0.17)	1.43 (± 0.17)	1.23 (± 0.13)	Ol + Wad	50 (± 10)	16	7	No
M3100 [h]	OL100	15.6	1160	0.07	2.3×10^{-5}	1.54 (± 0.13)	1.50 (± 0.15)	1.58 (± 0.24)	——	Ol + Wad + Rin + Fe-rich phase + Si-rich phase	—— [i]	1	24	Fault
P-T-t path#3														
M2670	OL92	15.2	1160	0.19	3.0×10^{-5}	1.78 (± 0.08)	1.75 (± 0.12)	2.14 (± 0.14)	——	Ol + Mj + Cpx + Wad	150 (± 10)	3	2	No
M2672	OL92	16.3	1160	0.11	4.0×10^{-5}	2.39 (± 0.08)	1.96 (± 0.15)	2.74 (± 0.15)	——	Ol + Mj + Cpx + Wad	190 (± 10)	13	6	No

[a] Average values of pressure around the yielding point. Error is within 0.2 GPa.

[b] Temperature at the center of the sample.

[c] Strain rate in the plastic deformation regime. Error is within 10 %.

[d] Yield strength evaluated from olivine diffraction patterns.

[e] Ol: olivine; Mj: majorite; Cpx: clinopyroxene; Wad: wadsleyite; Rin: ringwoodite

[f] Water content in the recovered samples. Initial water contents are 70 and 80 wt. ppm for the OL100 and OL92 samples, respectively.

[g] N: Total number of AE events from the inside (in) or outside (out) of the sample.

[h] Final blow out.

[i] Not analyzed.